Wave-phase dependence of Reynolds shear stress in the wake of fixed-bottom offshore wind turbine via quadrant analysis

C. Mouchref, B. Viggiano, O. Ferčák, J. Bossuyt, N. Ali, C. Meneveau, D. Gayme, and R. B Call Department of Mechanical and Materials Engineering, Portland State University, Portland, OR 97201, United States

69

70

²⁾Max Planck Institute for Dynamics and Self-Organization, Am Faßberg 17, 37077 Göttingen, Germany

³⁾Department of Mechanical Engineering, Johns Hopkins University, Baltimore, MD 21218, United States

I. ABSTRACT

There has been an increase in recognition of the important role that the boundary layer turbulent flow structure has on wake recovery and concomitant wind farm efficiency. Most research thus far has focused on onshore wind farms, in which the ground surface is static. With the expected growth of offshore wind farms, there is increased interest in turbulent flow structures above wavy, moving surfaces and their effects on offshore wind farms. In this study, experiments are performed to analyze the turbulent structure above the waves in 10 the wake of a fixed-bottom model wind farm, with special emphasis on the conditional averaged Reynolds stresses us-12 ing quadrant analysis. Phase-averaged profiles show a corre-13 lation between the Reynolds shear stresses and the curvature of the waves. Using quadrant analysis, Reynolds stress de-15 pendence on wave phase is observed in the phase-dependent 16 vertical position of the turbulence events. This trend is primarily seen in quadrants I and III (correlated outward and in-18 ward interactions). Quantification of the correlation between 19 the Reynolds shear stress events and the surface waves provides insight into the turbulent flow mechanisms that influ-21 ence wake recovery throughout the wake region and should 22 be taken into consideration in wind turbine operation and 23 placement.

II. INTRODUCTION

26

27

28

29

31

32

35

36

37

As more wind turbines are being placed offshore, additional design considerations must be made due to drastically different environmental conditions in comparison to onshore turbines. One must take into account environmental loading from waves, currents, and tides¹. Offshore wind is highly dependent on dynamic interactions between ocean waves and the atmospheric boundary layer (ABL). Locally generated short waves can be regarded as moving surface elements that affect the ABL through surface friction. Interaction between ocean waves and the ABL transfers momentum and energy to the mean airflow which influences the vertical wind speed profile and induces oscillatory motion².

The loss of momentum within the wind turbine wake negatively impacts power extraction and increases fatigue loading in downstream turbines.^{3,4}. Power extraction of the wind turbines in a row decrease moving farther downstream, which can significantly reduce the overall power output of the wind farm⁵. In a numerical study conducted by Yang, Meneveau,

and Shen⁶, downwind swells were found to have a considerable effect on power extraction and power output in offshore wind turbines.

Wave dependence can be detrimental to the life cycle of the turbine⁵. Wake dynamics behind a single turbine have a significant influence on performance and reliability⁷. Shear stress profiles in the near-field can provide insights used for control strategies to maximize power extraction. In the far-field, shear stress profiles are used to address the effect of the wake on fatigue loading of downstream turbines and the environment⁸. Therefore, understanding the dependence of waves on Reynolds shear stress profiles has the potential to make designing wind turbines for fatigue loading more effective and therefore contributing to a longer turbine lifetime and lower overall cost for offshore wind.

A number of analytical techniques are available which characterize the dynamics of a turbulent boundary layer. One technique, which provides valuable insight into momentum transport and Reynolds stress composition, is quadrant analysis. Quadrant analysis has been applied to turbulent boundary layer flow over rough walls^{9,10}, air-sea interactions over wind generated surface waves¹¹, the wake behind a cylinder^{12,13}, and flow over plant canopies. Yue et al. 14 and Zhu et al. 15 employed quadrant analysis to condition results of a large eddy simulation over a mature cornfield. Both studies found that sweeps (i.e. motions in which faster than average streamwise velocity moves downward) and ejections (i.e. when fluid with slower than average streamwise velocity moves upward) played a dominant role in turbulent kinetic energy evolution inside the canopy. A dominance of sweeping events and ejections was also observed in the wake of a static wind turbine array¹⁶. In a study conducted on a three by three model wind turbine array¹⁷, results showed that in an infinite array of turbines, Reynolds shear stress becomes the dominant mechanism for providing kinetic energy to the turbines. Viestenz and Cal ¹⁸ used quadrant analysis to characterize turbulent velocity statistics of the wake flow. Results showed that sweeps and ejections are dominant above the hub height while inward and outward interactions (positively and negatively correlated velocity interactions, respectively) are more influential below the hub height. This study also found that sweeping events tend to decrease above the top tip, in contrast to the increase of ejections, which were found to occur above the top tip. A study by Buckley and Veron 11 of turbulent airflow over wind generated surface waves shows an intense wave-phase dependent modulation by the wave field on the turbulence in the airflow. Upwind and downwind of the wave crests there is a dominance of outward and inward events. Additionally, it was noted that there was a similar frequency of occurrence for all quadrants events above crests and a very slight dominance of ejections and sweep events over troughs. Currently, little is known about the characteristics of the external flow structures that influence kinetic energy entrainment 19. Further characterization of the Reynolds stress should be performed by analyzing the fluctuating components of the velocity.

92

101

102

104

105

107

108

110

111

113

114

115

116

119

120

122

125

126

127

130

131

132

133

134

137

138

139

140

142

143

145

An additional challenge for offshore wind farms is the dynamic coupling of the ocean-wind and waves. Wind speed in the lower portion of the air-water boundary layer alternates (fast wind above the swell trough and slow wind above the swell crest) resulting in oscillatory wind speed due to wave propagation. It was found that an upward flux of kinetic energy due to the accelerating wind above the swell increases the extracted wind power in offshore turbines at wind speeds of 7 m/s and 10 m/s¹⁶. Yang, Meneveau, and Shen²⁰ created a dynamic model to represent small-scale unresolved wave motions as roughness elements in the context of wall modeled large eddy simulations of offshore wind farms. They found that "waves have an appreciable effect on the wind farm performance". In order to further characterize wave phase dependence, Xiao and Yang 21, performed a triple decomposition of the turbulent fluctuations and the phase averaged mean to define an instantaneous phase-averaged dependent fluctuation term. Additionally, in a study utilizing direct numerical simulations and triple decomposition, there was a dependence on spanwise wave-coherent velocity and vertical air velocity that was found to be in phase with the wave form²². Understanding the dynamic coupling between ocean waves and Reynolds shear stress can provide a better insight of offshore wind site conditions.

Ferčák *et al.* ⁵ performed a similar analysis on the same dataset used in this paper, focusing on the phase-dependent dynamics of the turbine wake. More specifically, velocity and Reynolds stress profiles were used to observe wave-phase dependence. In our analyses, we further study the Reynolds shear stress by categorizing the fluctuations using quadrant analysis to reveal how the direction of the flow is affected by wave phase.

Further complications can occur for floating turbines whose motion can be correlated with the wave motion. In the present study, we focus on the problem of fixed-bottom offshore turbines and more specifically on the structure of Reynolds stress distributions in the wake of a fixed wind turbine above moving waves. The data used in this study is generated in a laboratory experiment with a single scaled wind turbine in a wind tunnel above a water tank, and measure- 188 ments are taken via particle image velocimetry (PIV). Using 189 these data, we analyze the modulations of the turbine wake 190 associated with laboratory surrogates of deep-water ocean 191 waves. Analytical descriptions are presented in section III, followed by details of the experimental setup and data processing techniques in section IV. Section V provides the first and second-order statistics of the flow field as well as conditional averages based on quadrant analysis. Concluding remarks are included in section VI.

III. WIND VELOCITY DECOMPOSITIONS

The exchanges in momentum within the boundary layer when a wind farm is present can be understood through the Navier-Stokes equation. It takes into account the force imposed by the turbines within the flow acting as momentum extracting elements. Results from Cal *et al.* ¹⁷ showed that the vertical gradients for the momentum flux in the wind turbine wake are significantly greater than the spanwise or streamwise gradients, thus only the vertical terms are considered in the momentum balance for this application. Based on this, the Reynolds-averaged Navier-Stokes equation for a steady and incompressible flow while neglecting viscous stress, is written in the streamwise direction as,

$$\overline{u}\frac{\partial \overline{u}}{\partial x} + \overline{v}\frac{\partial \overline{u}}{\partial y} = -\frac{1}{\rho}\frac{d\overline{p}}{dx} - \frac{\partial}{\partial x}\overline{u'u'} - \frac{\partial}{\partial y}\overline{u'v'} - \overline{f_x}, \quad (1)$$

where u, and v, are the instantaneous streamwise and vertical velocities respectively in the x and y directions. Once the Reynolds decomposition and averaging has been performed, primes indicate turbulent fluctuations and overbars indicate time-averaging. The term $\overline{u^iv^i}$ is the Reynolds shear stress and accounts for vertical recovery of momentum in the wake¹⁶. The fluid density is represented by ρ and $\overline{f_x}$ represents the thrust effect of the wind turbine which acts only in the region where wind turbines are located. Viscous terms are neglected since these have negligible effect on mean momentum at large Reynolds numbers away from solid boundaries. Viscous forces from the turbine blades are accounted for in f_x .

Given that the lower boundary now contains a free surface, wave-phase dependence of Reynolds stresses become of interest. Phase-averaging techniques are used to decompose the velocity field as is presented in Buckley and Veron ²³. Thus, instantaneous streamwise (u) and wall-normal (v) velocity fields can be conditioned according to their phase, ϕ , where ϕ is defined in the interval $[-\pi, \pi]$, from wave trough to wave trough, with increasing phase in the downwind direction and $\phi = 0$ at the crest²³. First, the individual instantaneous phase-conditioned velocity fields, $u_{\phi}(x, y, z, t)$, can be decomposed to find the time-averaged component and the turbulent deviations,

$$u_{\phi}(x, y, z, t) = \overline{u}_{\phi}(x, y, z; \phi) + u'_{\phi}(x, y, z, t). \tag{2}$$

A dependence on ϕ is introduced as the wave phase, while x, y and z are the streamwise and wall-normal and spanwise location, respectively. The phase averaged mean velocity, $\overline{u}_{\phi}(x,y,z;\phi)$, can be further decomposed into the ensemble mean (or average of all phases), $\overline{u}(x,y,z)$ and phase averaged deviations $\widetilde{u}(x,y,z,\phi)$ according to:

$$\overline{u}_{\phi}(x, y, z; \phi) = \overline{u}(x, y, z) + \widetilde{u}(x, y, z, \phi). \tag{3}$$

The phase-averaged mean is not resolved from the ensemble mean, it is a composition of the ensemble mean and

the phase-averaged deviation. Substitution of Eq. (3) into Eq. (2), results in triple decomposition:

196

197

198

201

202

204

206

207

208

209

212

214

216

217

219

220

222

225

226

$$u_{\phi}(x, y, z_0, t) = \overline{u}(x, y, z_0) + \tilde{u}(x, y, z_0, \phi) + u'_{\phi}(x, y, z_0, t),$$
 (4)

providing an indication that these quantities are related. Here, z_0 is introduced to denote that the velocity is taken at a given plane directly behind the turbine. Therefore additional conditioning of the velocity signals is required to quantify the influence of the wave-wind interface on the wake dynamics.

Analysis of dominant contributions to the Reynolds shear stress can be characterized through a conditional sampling technique called quadrant analysis 16,24 . Velocity fluctuations are characterized into four types of events based on the respective signs of streamwise and wall-normal fluctuating velocity components designated as followed: Q1, outward interaction ($u_\phi',v_\phi'>0$); Q2, ejection ($u_\phi'<0,v_\phi'>0$); Q3, inward interaction ($u_\phi',v_\phi'<0$); and Q4, sweep ($u_\phi'>0,v_\phi'<0$). These four events can be represented visually by creating a plane spanned by orthogonal axes with u_ϕ' on the abscissa and v_ϕ' as the ordinate see figure 1^{18} .

$$\langle u'_{\phi_k} v'_{\phi_k} \rangle = \frac{1}{N} \sum_{k=1}^{N} I_m(u'_{\phi_k}, v'_{\phi_k}) u'_{\phi_k} v'_{\phi_k}$$
 (5)

where m denotes the quadrant, i.e., m=1, 2, 3, and 4, k is a given snapshot signal and N is the total number of snapshots in the data set. The function $I_m(u'_{\phi_k}, v'_{\phi_k})$ is defined as,

$$I_m(u'_{\phi_k}, v'_{\phi_k}) = \begin{cases} 1, & \text{If } (u'_{\phi_k}, v'_{\phi_k}) \text{ is in quadrant } m \\ 0, & \text{otherwise.} \end{cases}$$
 (6)

Quadrant events can be physically interpreted as revealing the directionality of the flow in comparison to the mean flow. For example, ejections represent turbulent bursts upwards at velocities slower than the mean, while sweeps represent turbulent burst downward in the positive streamwise direction 16. Events in quadrants 2 and 4 cause a downward convection of streamwise momentum while quadrants 1 and 3 provide an upward flux 18.

231

232

IV. EXPERIMENTAL SETUP

Experiments were performed at Portland State University in the closed loop wind tunnel in which the floor was replaced by a 0.3 m deep water tank to replicate conditions impacted by deep open waves. The tank spanned the entire experimental test section of the tunnel which is 0.8 m by 1.2 m in cross-section and 5 m in length. A scaled wind turbine was placed on a stiff support within the water tank, situated just below the surface of the water, see figure 2. The turbine has a diameter, D, of 0.15 m, resulting in a geometric scaling ratio to a full size wind turbine of 1:600, based on a rotor design following the work of Odemark and Fransson 25. A tip speed ratio of 5 was chosen for the experiments with a turbine power coefficient $c_p \approx 0.25$ at this rating.

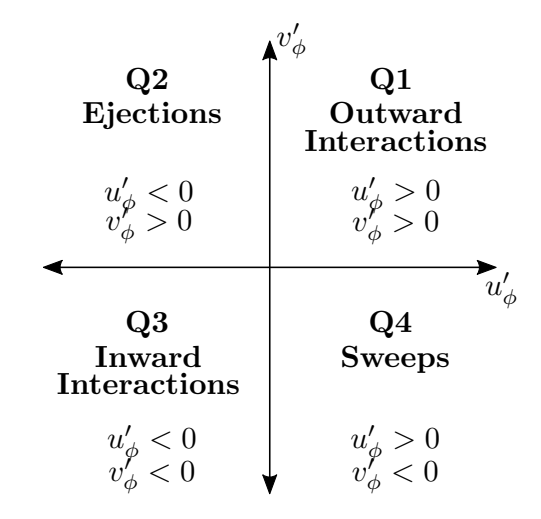


FIG. 1. Definition of the four quadrant for the wake of the wind turbine based on the phase-dependent fluctuating velocities u'_{ϕ} and v'_{A} .

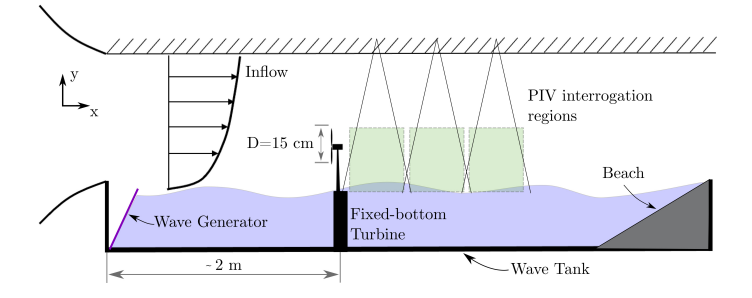


FIG. 2. Experimental setup of the wind tunnel (not to scale). *Reproduced with permission from J. App. Ener.* 309, 118358(2022). Copyright 2022 Elseiver.⁵

At the entrance of the tunnel test section a wave paddle produces scaled deep-water waves. The wave and wind interface was measured using laser induced fluorescence (LIF) visualization and the wave height and frequency was extracted for each snapshot. Finally, a damper was placed at the end of the tunnel to absorb incoming waves. Three conditions were used to quantify the impact of wave frequency on wake effects of the turbine. Two active conditions and one passive (no wave paddle) condition, with parameters of the two active cases presented in table I. The free stream wind tunnel speed varied from 2.5 ms⁻¹ to 5.5 ms⁻¹. No wave breaking occurred during the experiments. The low frequency wave has characteristics of a more typical ocean wave while the high frequency wave is not typically observed in normal ocean conditions. The two cases were chosen in order to compare differences in two extreme wave frequency conditions.

The inflow conditions, measured without the wind turbine in the wind tunnel, fit well into an idealized neutral turbulent boundary layer common for wind tunnel experiments ^{17,26}. The roughness length, found by fitting log-law to the mean

velocity profile, is 0.5×10^{-4} and 0.6×10^{-4} m for the long 302 wave and short period wave conditions respectively. The 303 friction velocity, using a von Karman constant of 0.4, was 304 found to be 0.27 and 0.26 m/s for the long wave and short pe- 305 riod wave conditions respectively. The turbulence intensity is 306 found to be 6-7% at hub height for the long period waves and 8% for the short period wave. The turbulent intensity values 308 for this experiment correspond well to turbulent values experienced offshore^{27,28} The integral length scale was calculated at hub height by integrating the spatial correlation function of the streamwise velocity in the horizontal direction from the PIV data is around 2cm-2.5cm at hub height. The integral length scale corresponds to 10 m in full scale with a scaling ratio of 1:600 or 2/15th of the rotor diameter of the wind turbine²⁹. Additional inflow conditions are discussed in more detail by Ferčák et al. 5.

In the present study, PIV was employed to measure snapshots of velocity fields. Three PIV planes of data were extracted at 1D, 2.5D and 4D downstream of the turbine with the measurement window parallel to the streamwise velocity, as shown in figure 2. Images were captured with a 4 megapixel CCD camera using a Nd:YAG double pulsed laser. A seeding generator aerosolized diethyl-hexyl sebacate into the the tunnel with constant density during the measurements. 3000 individual snapshots were taken at 4Hz for each of the PIV planes and inflow conditions. The data³⁰ were processed in Davis 8.4 using a cross-correlation algorithm with one pass with an interrogation area of 64×64 pixels and 50% overlap followed by a pass with an interrogation size of 32×32 pixels.

V. RESULTS

248

251

252

254

255

257

258

260

261

263

265

266

268

269

271

272

274

275

278

280

283

285

288

289

291

292

295

297

300

301

The spatial distribution of measured mean horizontal and vertical velocity and Reynolds shear stress distribution are shown in Figs. 3. As in all subsequent figures, the solid black line represents the location of the rotor hub. The dashed lines represent the location of the top and bottom tip of turbine blades.

Figure 3 shows normalized fields using u_{∞} , the free-stream ³⁴² velocity, as scale for velocity, i.e. the figure depicts the 343 ensemble-averaged normalized streamwise velocity \overline{u}/u_{∞} , ³⁴⁴ wall-normal velocity \overline{v}/v_{∞} , and Reynolds stress $\overline{u'v'}/u_{\infty}^2$ at a 345 wind tunnel speed (v_L) of 2.5 m/s and wave frequency $(\omega_{1,25})$ 346 of 1.25 Hz. The x and y coordinates are normalized by the diameter (D) of the rotor. Inflow is from left to right and the turbine rotor is located at x/D = 0. The region of x/D values was 349 chosen to capture the full range of behaviors behind the wind 350 turbine. Extraction of energy from wind across a turbine ro- 351 tor produces a wake region downstream with reduced velocity and increased turbulence. The streamwise velocity con- 353 tour shows a canonical wake profile with a region of reduced 354 momentum directly behind the turbine rotor, which recovers 355 as it moves downstream. Increased velocity, reaching nearly 356 that of the free stream is reached quickly above the top tip of 357 the turbine. A slight increase in \overline{u} is also observed below the 358 bottom tip. Negative wall-normal velocity is observed behind 359 the turbine rotor where the fluid is entrained from above the top tip during wake recovery. Upward (positive) wall-normal velocity is equally observed as fluid is entrained from below the bottom tip. Time-averaged streamwise, wall-normal velocity, and velocity recovery are discussed in more detail by Ferčák *et al.* ⁵.

For the normalized turbulent shear stress, $\overline{u'v'}/u_{\infty}^2$, shown in Figure 3(c), there is a region at the wake center where the shear stress is zero with positive stresses below and negative stresses above. The large streaks of stresses are acute features located at top tip and bottom tip of the turbine induced by helical tip vortices. $\overline{u'v'}/u_{\infty}^2$ is negative above the rotor characterizing downwards transfer of streamwise momentum (or flux of kinetic energy in the mean flow if multiplied by mean velocity \overline{u}^{17}), while $\overline{u'v'}/u_{\infty}^2$ is positive below the rotor characterizing an upward transfer of momentum and kinetic energy³¹. As the wake recovers farther downstream, regions of positive and negative shear stress diffuse and occupy a larger vertical range.

For comparison between the different cases in the experiments, the Reynolds stress for all cases is presented as profiles averaged in space over the streamwise locations for 1 < x/D < 2.5 and over all time samples. The total Reynolds stress profiles (i.e., prior to phase averaging) for all considered inflow conditions are shown in Figure 4. v_L corresponds to a wind tunnel speed of 2.5 m/s and v_H corresponds to a wind speed of 5.5 m/s. ω_0 , $\omega_{1.25}$, and $\omega_{2.00}$ correspond to the wave frequency of 0Hz, 1.25Hz, and 2.00Hz respectively. All of the inflow conditions induce consistent profiles and closely resemble the no-wave boundary condition $(v_1 \omega_0)$. Slightly larger deviations from the no wave condition are seen in the high frequency wave cases ($\omega_{1.25}$), compared to the low frequency wave cases ($\omega_{2,0}$). For the high frequency cases, the low wind speed case has slightly larger deviations from the no wave condition in the region between the rotor hub and wave. The disruption of airflow across the turbine rotor and blades produces a negative shear stress above the rotor and a positive shear stress below the rotor. The stress profile appears strongly modulated (with visible undulations) in the near field, the PIV plane extracted at 1D downstream of the turbine and closest to the inflow, then as turbulence grows in strength moving downstream, the wake begins to recover and shear stress magnitude increases into an expanding area as these undulations disappear.

332

334

Figure 5 depicts the four wave-phase (ϕ) averaged Reynolds stress profiles $(u'_{\phi_i}v'_{\phi_i})$ at quarter wave increments for the long wave condition $(\omega_{1.25})$ and low wind tunnel speed (v_L) of 2.5 m/s. The lower wind tunnel speed cases were chosen for further analysis in that the effects of the wave-wind interactions are more prominent than those observed in the high wind tunnel speed cases. The motion of the wave at each phase is determined by the relative position of the crest and the trough of the wave depicted by the cropped white region at the bottom of the image. Similar to the Reynolds stress contour seen in Figure 3, there is a region where the shear stress is zero at the wake center that marks a switch from positive to negative shear stress. The wake center deviates in the shear profiles and follows the concavity of

Wind specs Wave specs Wind speed [m/s] Reference name Wave condition Frequency [Hz] Period [s] Amplitude [m] Speed [m/s] Wavelength Wave Age[m] No wave $v_L \omega_0$ 2.5 $v_H \omega_0$ 5.5 2.5 Long 1.25 $0.8 (\pm 0.01)$ 0.013 $1.2 (\pm 0.08)$ $1.00 (\pm 0.06)$ 0.48 $v_L \omega_{1.25}$ $v_H \omega_{1.25}$ 5.5 0.22 $v_L \omega_{2.0}$ 2.5 Short 2.00 $0.5 (\pm 0.01)$ 0.020 $0.7 (\pm 0.03)$ $0.36 (\pm 0.02)$ 0.28 5.5 0.13 $v_H \omega_{2.0}$

TABLE I. Wave tank experimental parameters.

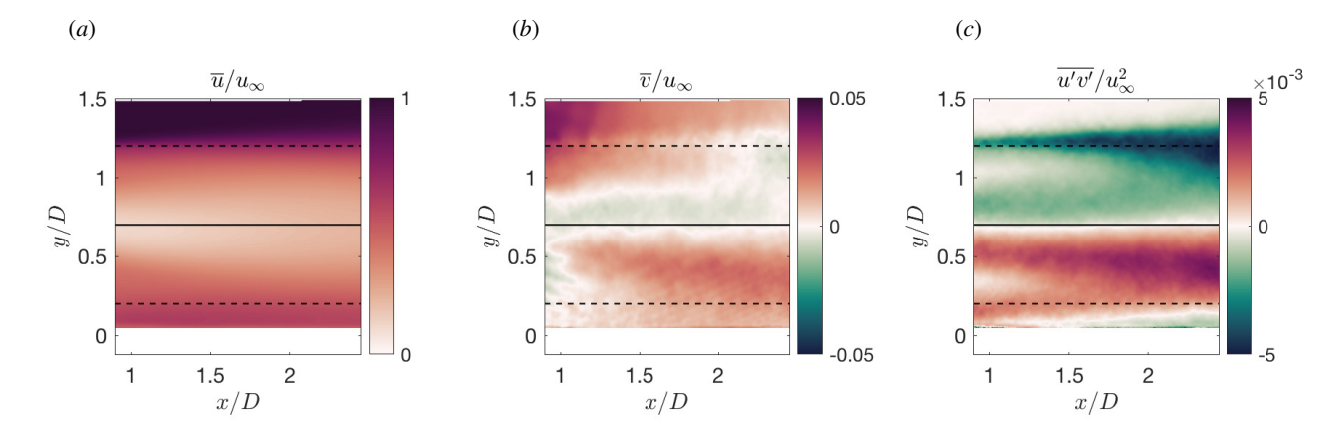


FIG. 3. Time averaged streamwise (a), wall-normal (b) velocities and Reynolds shear stress (c) for the $v_L \omega_{1.25}$.

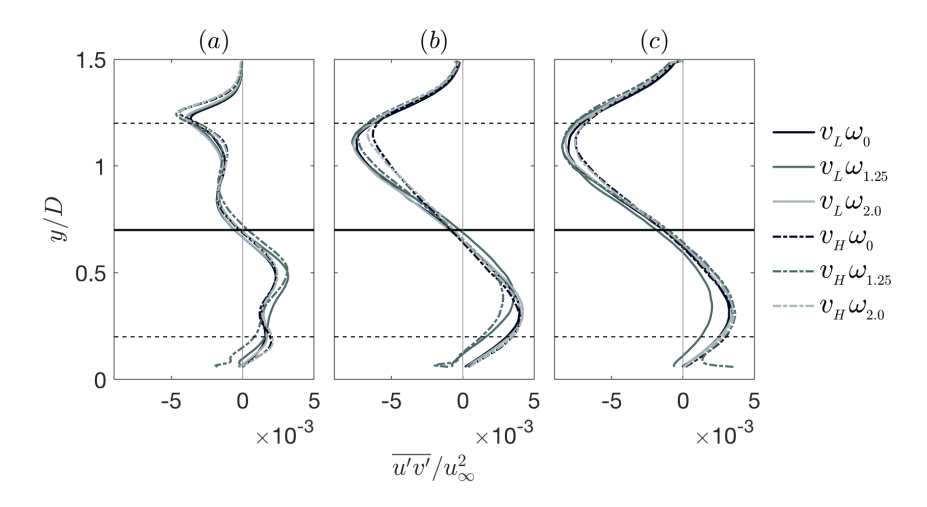


FIG. 4. Profiles of the Reynolds stress, $\overline{u'v'}/u_{\infty}^2$ for all cases as a function of wall-normal location. The profiles are averaged in time and in space from namely; (a) 0.9 < x/D < 2.5, (b) 2.5 < x/D < 3.9 and (c) 3.9 < x/D < 5.3.

the wave shape, indicating a phase dependence.

360

361

363

364

366

369

370

The positive and negative shear stress regions above and below the wake center also experience a phase dependence and align with the wave phase profile. Areas of positive shear stress are observed at the leading edge of the wave followed by a negative shear on the trailing edge of the wave, evidence of wave-induced shear stress due to the wind aloft. The wave-induced shear stress suggests that the wind-wave interactions play an important role locally. There are extended tails of negative shear stress events that follow the wave, wherein the flow is being entrained and advancing the flow. The phase 377

dependence of the shear stress structures can be utilized to maximize the efficacy of control strategies and turbine spacing to increase power production of successive turbines³².

To quantify the effects of the Reynolds stress per component, the flow field is conditioned further to isolate and characterize these trends. Figure 6 utilizes quadrant analysis to depict the ensemble Reynolds stress for the long wave condition and low wind tunnel speed of 2.5 m/s in the near-field $(v_L\omega_{1.25})$. Recall that quadrant events can be physically interpreted as revealing the directionality of the flow in comparison with the mean flow 18, i.e., advancing or impeding

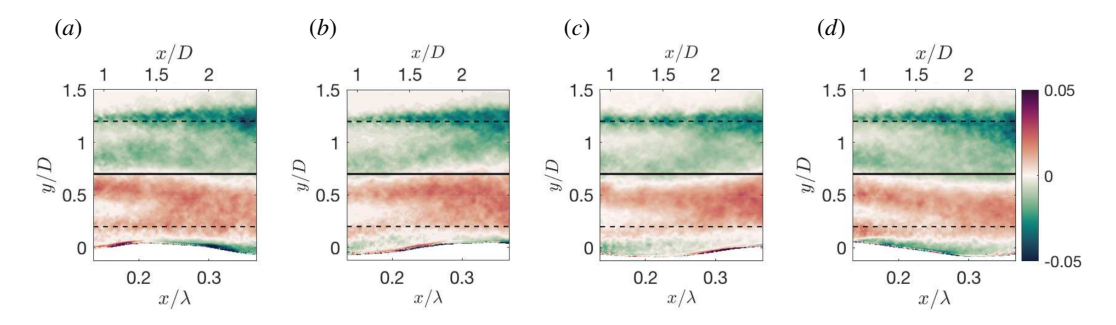


FIG. 5. $\langle u'_{\phi_i} v'_{\phi_i} \rangle$ for the four phases: (a) ϕ_1 , (b) ϕ_2 , (c) ϕ_3 and (d) ϕ_4 for the case $v_L \omega_{1.25}$ for the near-field location. The y axis is normalized by the D while the x locations are normalized D downstream as well as by the wave number, λ .

the flow, entraining or ejecting. Quadrants 2 and 4 have peak magnitudes slightly larger than quadrants 1 and 3. A dominance of ejections and sweeps (quadrants 2 and 4) are observed behind top tip of the turbine blade and the nacelle, which contributes to the negative Reynolds stress in those regions. This is consistent with the general trend that sweep and ejection events are prominent in high shear regions of boundary layer flows since streamwise and wall-normal velocity fluctuations are typically anti-correlated (i.e., leading to large magnitudes of -u'v')³³. Events in quadrants 1 and 3 are localized between the bottom tip of the turbine blade and near the wave. This is consistent with results reached by Viestenz and Cal¹⁸, where sweeps and ejections are dominant above the hub height while inward and outward interactions are more influential below the hub height. Therefore, the flow being entrained from the free stream is dominated by events where fluctuations possess opposing sign (Q2 and Q4) or are therefore inversely correlated. Meanwhile, below the bottom tip and associated strongly associated with the wave motion, dominating events carry the same sign (Q1 and Q3), where the interactions (inward and outward) are much more promi-

382

384

385

387

388

390

301

392

393

396

397

399

400

402 403

404

405

407

408

410

412

413

415

416

418

419

423

424

426

427

On-shore turbine wake flow presents large structures at the top tip in Q2 and Q4¹⁶, as is observed for the fixed bottom turbine cases presented in figure 6 as well. In addition, structures are observed at the bottom of the interrogation area and cause inward and outward interactions which are less commonly observed in on-shore turbine wakes. This addition is likely due to wave-wind interactions causing correlation of the streamwise and spanwise fluctuations.

To interpret the effects of the phase on the conditioned flow, quadrant analysis is applied and profiles are compared. Figures 7 and 8 depict quadrant analysis of the Reynolds shear stress profiles $(u'_{\phi_i}, v'_{\phi_i})$ at a low wind tunnel speed (v_L) of 2.5 m/s at long $(\omega_{1.25},$ figure 7) and short $(\omega_{2.00},$ figure 8) wave conditions for all four phases. The profiles are obtained by time averaging then spatial averaging over the respective streamwise locations to investigate near to far-wake dynamics. The profiles are normalized by the averaged magnitude of $\langle |\overline{u'v'}| \rangle$ for each given case. Reynolds shear stress in all four quadrants and all conditions dissipates moving downstream as undulations disappear and magnitude increases. Negative peak magnitudes occur in quadrants 2 and 4 between the rotor and the top tip of the turbine blade. Positive

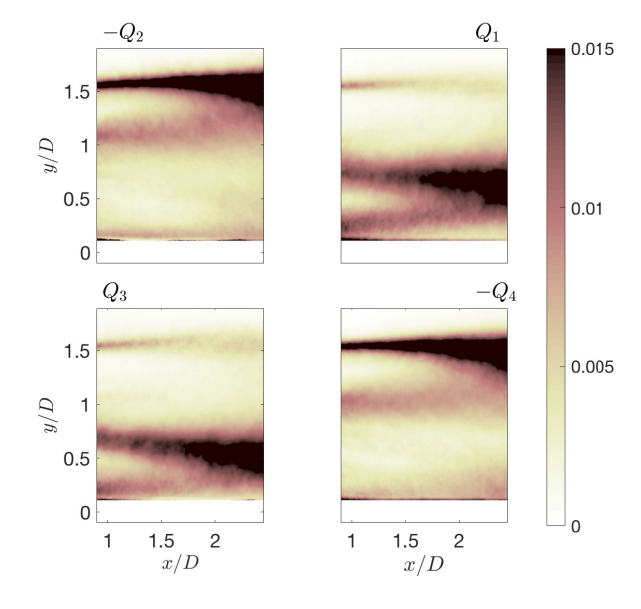


FIG. 6. Quadrant conditioned contours of the near field of the case $v_{L} \omega_{1.75}$ for the total stress $\overline{u'v'}$.

peak magnitudes occur in quadrants 1 and 3 between the the water surface and the bottom tip of the blade. A phase dependence can be seen in all four quadrants as the stress profiles are shifted vertically relative to the stress profile of the condition with no-wave $(v_L\omega_0)$. For the long wave condition depicted in figure 7, deviations from the no-wave condition are seen in quadrants 1 and 3 due correlation with wave phase. As the fluid moves across the long wave at the interface, it exhibits strong vertical velocity fluctuations that coincide with the slope of the wave, increasing the conditioned stresses at the near wave heights behind the turbine, increasing and decreasing the events in Q1 and Q3 in comparison to the no wave condition. Deviations due to wave phase seen in quadrants 2 and 4, located much farther from the air water interface, are smaller than deviations in quadrants 1 and 3. For the short wave condition depicted in figure 8, larger phase deviations are seen in quadrant 2 and 4 for the short wave condition than the long wave conditions. In addition, quadrants 1 and 3 have less phase dependence for the short wave than the long wave. The wave phase dependence of the short wave $(v_L\omega_{2.0})$ observed in Q2 and Q4 can be attributed

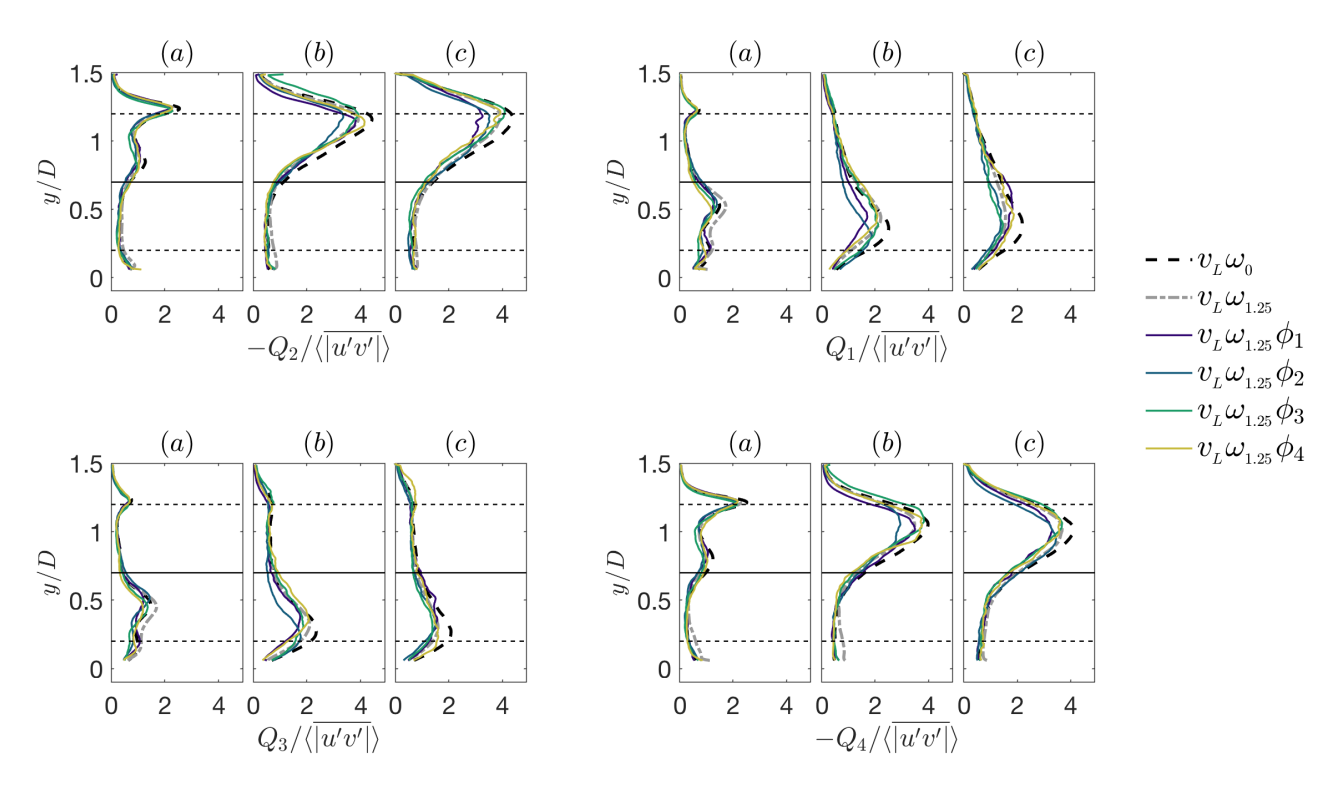


FIG. 7. Comparison of the profiles of the quadrant analysis, for all phases of $v_L \omega_{1.25}$. The case with no wave paddle input is included for comparison as well. The profiles are summed over their downstream locations of (a) 0.9 < x/D < 2.5, (b) 2.5 < x/D < 3.9 and (c) 3.9 < x/D < 5.3 and all curves are normalized by spatially averaged Reynolds stress.

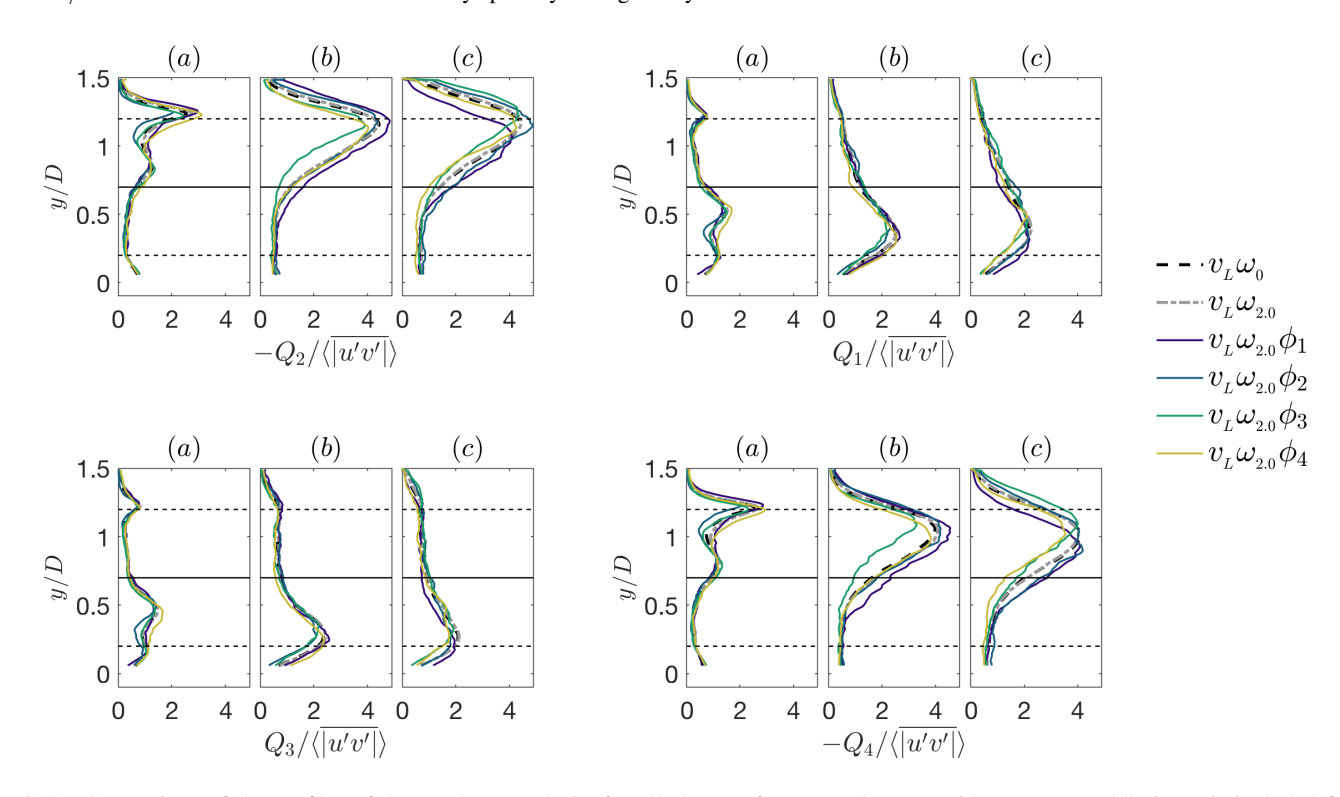


FIG. 8. Comparison of the profiles of the quadrant analysis, for all phases of $v_L \omega_{2.0}$. The case with no wave paddle input is included for comparison as well. The profiles are summed over streamwise locations of (a) 0.9 < x/D < 2.5, (b) 2.5 < x/D < 3.9 and (c) 3.9 < x/D < 5.3 and all curves are compensated by the average of the Reynolds stress of each respective case.

on the wake behavior and therefore produces clear variation of the above hub height as a function of the wave phase. In all four quadrants, larger peak shear stress values are seen in the 2.00 Hz wave condition(figure 8) compared to the 1.25 wave Hz condition(figure 7). For onshore wind, peak sweep and ejection events show magnitudes of stress approximately 70% higher than that of the interaction events (Q2 and Q4) show magnitudes of stress approximately 45-60% percent higher than that of the interaction events (Q1 and Q3). Higher magnitude of interaction events is likely due to interactions at the air-water interface.

452

453

455

456

457

458

459

461

462

465

466

467

468

471

475

477

480

481

483

486

487

489

490

492

493

495

496

498

499

501

502

504

505

507

508

The dependence on the wave for increased stresses near the wave-wind interface could cause increased vibrations and fatigue to the turbines and the mast when operating in offshore, fixed bottom conditions. This is most noticeable by the large stresses observed in the far-field, the PIV plane 4D downstream of the turbine and farthest away from the inflow, for Q1 and Q3 in figures 7 and 8, which occur just above the bottom tip of the rotor. Q1 and Q3 turbulent events can influence power production of consecutive turbines. Understanding how phase influences Reynolds shear stress can provide insights on wake recovery which can be used to maximize power extraction in downstream turbines through wake deviation, control strategies, and turbine spacing.

Differences in sweeps and ejections are correlated to gradients of second-order correlation terms, and can therefore utilized in second-order closure models³⁴. Figure 9 depicts the difference between the Reynolds stress profiles of Q2 (ejections) and Q4 (sweeps). Ejections and sweeps dominate the flow at different spots. When the difference is negative, ejections dominate the flow, and when the difference is positive sweeps dominate the flow. The difference in magnitude is positive between the rotor center and the top tip due to the fact that sweeps increase in that range. Above the top tip, sweeps decrease and ejections increase making the difference magnitude negative in this region. A slight phase dependence is seen in the difference between Q2 and Q4 as the stress profiles are offset from the no wave condition.

Figure 10 contains the difference between the Reynolds 546 stress profiles of Q1 (outward interactions) and Q3 (inward 547 interactions). When the values of the profile are positive, 548 outward interactions dominate the flow and when the profile 549 is negative, inward interactions dominate the flow. The 550 strong correlation between these events and wave phase is 551 seen as the phase averaged stress profiles deviate greatly 552 from the no-wave condition. The difference profile switches 553 signs and becomes positive as outward interactions dominate 554 the flow between the bottom tip and the top tip with a mag- 555 nitude that peaks close to the rotor height. Phase dependence 556 alters the location of quadrant events 1 and 3 as well as 2 557 and 4 relative to one another observed in Figs. 9 and 10. 558 Quantifying the difference magnitude between Q2 and Q4 559 events as well as Q1 and Q3 events provides information on 560 the location of the flow mechanisms, which influence wake 561 recovery.

VI. CONCLUSIONS

This study focused on the turbulent flow structure in the wake of a scaled fixed-bottom turbine at two different wind speeds and three wave conditions. PIV measurements were collected in a closed loop wind tunnel at three downstream locations to generate velocity fields and detect instantaneous wave profiles for phase averaging. Phase-averaged shear stress profiles were divided into four quadrants based on the respective signs of the fluctuating streamwise and vertical velocity components to characterize the dominant contributions to Reynolds shear stress. Results show that wave phase influences the vertical location of the wake center and stress fields. The wake center and stress field were shifted vertically based on the concavity of the wave below. Knowledge of wave-phase dependence can help build a better understanding of complex dynamics experience by offshore wind turbines.

Conditioning of the Reynolds shear stress into four quadrants shows that in addition to sweeps and ejections between the hub and the top tip, as commonly seen in onshore wind turbine wakes, there is also an increase in magnitude of inward and outward interactions near the air-water interface.

Profiles depicting quadrant analysis for all four phases demonstrate wave phase dependence in all four quadrant events as stress profiles are shifted in the vertical direction and locations of peak magnitudes vary from the no wave condition $(v_L \omega_0)$. Differences in magnitude when comparing the long wave and short wave boundary conditions were seen. For the long wave inflow condition, slight deviations from the the no wave condition can be seen in quadrants 1 and 3, in addition to smaller deviations seen in quadrants 2 and 4. Oppositely for the short wave condition, more prominent phase deviations are seen in quadrant 2 and 4 than quadrants 1 and 3. The deviations are small, but still show wave-phase dependence. Inward and outward interactions had a higher magnitude compared to results from onshore wind, showing a link between these correlated stress events and wind-water interactions experienced offshore.

Quantification of differences in ejections and sweeps (Q2-Q4) showed that sweeps increased in between the rotor and top tip. Above the top tip sweeps decrease and ejections increase. Slight phase dependence was seen as the difference profile deviated from the no wave case. The difference in magnitude between quadrants 1 and 3 deviates from the no wave condition due to a phase dependence near the air-water interface where these stress event occur. Inward interactions (Q3) dominate the flow above the top tip and below the bottom tip of the turbine blades. Outward interactions (Q1) dominate the flow between the bottom tip and top tip with a maximum close to the rotor hub.

The persistence of the Reynolds shear stress in the far-field indicates downstream turbines could be affected by structural loads as the Reynolds stresses have a preference with respect to the specific events. Since these events are preferential in nature, they can be associated with unbalanced loadings on the blades which could lead to increased fatigue³⁵. Further, if these stresses are undesirable, distances and placement could be altered to avoid such stresses. Reynolds shear stress undu-

564

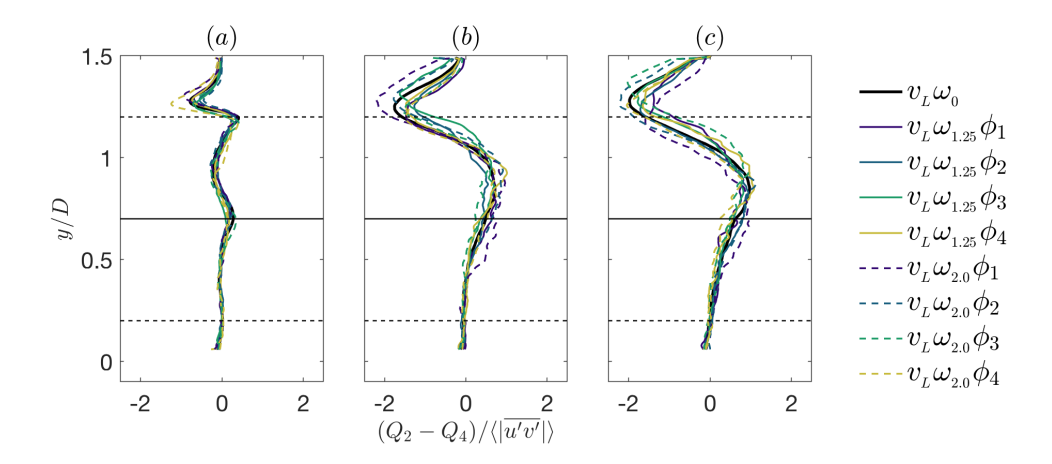


FIG. 9. Quantification of the ejections and sweeps associated with the low-speed cases. Profiles are averaged in space over streamwise locations of (a) 0.9 < x/D < 2.5, (b) 2.5 < x/D < 3.9, and (c) 3.9 < x/D < 5.3.

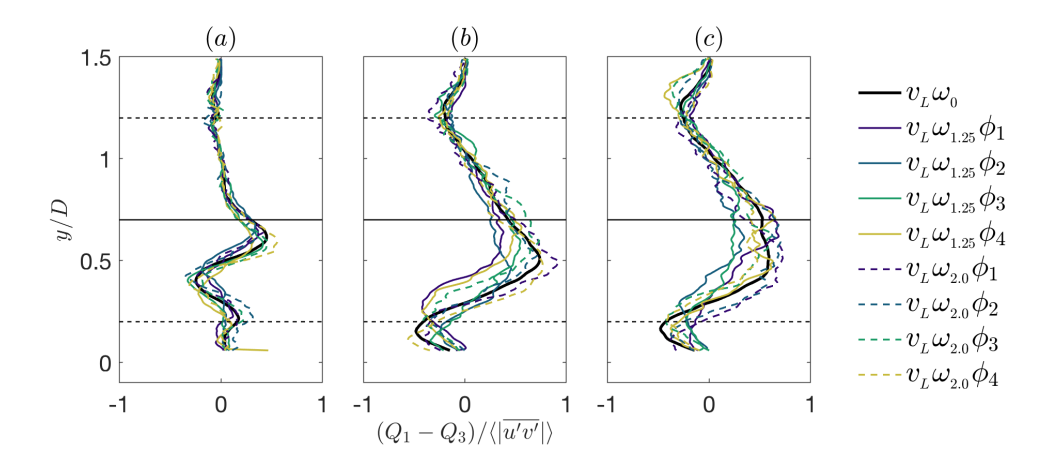


FIG. 10. Differences of the inward and outward interactions based on the quadrant analysis for all low-speed cases considered. Profiles are spatially averaged over respective streamwise locations of (a) 0.9 < x/D < 2.5, (b) 2.5 < x/D < 3.9, and (c) 3.9 < x/D < 5.3.

591

592

593

505

lations need to be considered for optimization, siting, modeling, and maximizing power production⁵. Waves induce a change in momentum direction observed through increased quadrant 1 and 3 events. Further experiments should be conducted to build off the findings of this study. This analysis focuses on dynamics behind one turbine yet a study could consider how these preferential events develop in a wind turbine array in the presence of waves, thus having possible implications in the power extraction process in the offshore wind farm.

VII. ACKNOWLEDGEMENTS

569

571

572

574

577

580

581

JB received funding from the Belgian American Education Foundation. DG and CM are supported by NSF (grant # CMMI 2034111). OF, ZS, JB and RBC are supported by NSF (grant # NSF-CMMI-2034160, NSF-CBET-2227263, and NSF-CBET-2037582).

VIII. REFERENCES

¹J.-T. Horn and B. J. Leira, "Fatigue reliability assessment of offshore wind turbines with stochastic availability," Reliability Engineering & System Safety **191**, 106550 (2019).

²A. D. Jenkins, M. B. Paskyabi, I. Fer, A. Gupta, and M. Adakudlu, "Modelling the effect of ocean waves on the atmospheric and ocean boundary layers," Energy Procedia **24**, 166–175 (2012).

³Y. Wang, W. Miao, Q. Ding, C. Li, and B. Xiang, "Numerical investigations on control strategies of wake deviation for large wind turbines in an offshore wind farm," Ocean Engineering **173**, 794–801 (2019).

⁴J. Bossuyt, M. F. Howland, C. Meneveau, and J. Meyers, "Measurement of unsteady loading and power output variability in a micro wind farm model in a wind tunnel," Experiments in Fluids **58**, 1–17 (2017).

⁵O. Ferčák, J. Bossuyt, N. Ali, and R. B. Cal, "Decoupling wind-wave-wake interactions in a fixed-bottom offshore wind turbine," Applied Energy 309, 118358 (2022).

⁶D. Yang, C. Meneveau, and L. Shen, "Effect of downwind swells on offshore wind energy harvesting—a large-eddy simulation study," Renewable Energy **70**, 11–23 (2014).

⁷P. McKay, R. Carriveau, D. S. Ting, and T. Newson, "Turbine wake dynamics," in *Advances in Wind Power* (IntechOpen, 2012).

- 8G. Marmidis, S. Lazarou, and E. Pyrgioti, "Optimal placement of wind turbines in a wind park using monte carlo simulation," Renewable energy
 33, 1455–1460 (2008).
- ⁹Y. Wu and K. Christensen, "Outer-layer similarity in the presence of a practical rough-wall topography," Physics of Fluids **19**, 085108 (2007).

608

609

625

626

627

628

636

637

638

- 10 K. P. Nolan and T. A. Zaki, "Conditional sampling of transitional boundary layers in pressure gradients," Journal of Fluid Mechanics 728, 306–339 (2013).
- i1 M. P. Buckley and F. Veron, "The turbulent airflow over wind generated surface waves," European Journal of Mechanics-B/Fluids 73, 132–143
 (2019).
- 614 12 R. Antonia and L. Browne, "Quadrant analysis in the turbulent far-wake 657 of a cylinder," Fluid dynamics research 2, 3 (1987). 658

656

677

- 616 ¹³G. Fabris, "Conditional sampling study of the turbulent wake of a cylinder.
 659 part 1," Journal of Fluid Mechanics 94, 673–709 (1979).
 660 660
- i4 W. Yue, C. Meneveau, M. B. Parlange, W. Zhu, R. Van Hout, and J. Katz,
 "A comparative quadrant analysis of turbulence in a plant canopy," Water resources research 43 (2007).
- 15 W. Zhu, R. Van Hout, L. Luznik, H. Kang, J. Katz, and C. Meneveau, 664
 "A comparison of piv measurements of canopy turbulence performed in 665
 the field and in a wind tunnel model," Experiments in fluids 41, 309–318
 (2006).
 - 16N. Hamilton, H. Suk Kang, C. Meneveau, and R. Bayoán Cal, "Statistical analysis of kinetic energy entrainment in a model wind turbine array boundary layer," Journal of renewable and sustainable energy 4, 063105 (2012).
- ¹⁷R. B. Cal, J. Lebrón, L. Castillo, H. S. Kang, and C. Meneveau, "Experimental study of the horizontally averaged flow structure in a model wind-turbine array boundary layer," Journal of renewable and sustainable energy 2, 013106 (2010).
- ¹⁸K. Viestenz and R. B. Cal, "Streamwise evolution of statistical events in a model wind-turbine array," Boundary-layer meteorology 158, 209–227
 (2016).
 - ¹⁹H. F. Kadum, D. Knowles, and R. B. Cal, "Quantification of preferential contribution of reynolds shear stresses and flux of mean kinetic energy via conditional sampling in a wind turbine array," Journal of Fluids Engineering 141 (2019).
- 20 D. Yang, C. Meneveau, and L. Shen, "Dynamic modelling of sea-surface roughness for large-eddy simulation of wind over ocean wavefield," Journal of Fluid Mechanics 726, 62–99 (2013).
- S. Xiao and D. Yang, "Large-eddy simulation-based study of effect of swell-induced pitch motion on wake-flow statistics and power extraction of offshore wind turbines," Energies 12, 1246 (2019).

- ²²G. Deskos, S. Ananthan, and M. A. Sprague, "Direct numerical simulations of turbulent flow over misaligned traveling waves," International Journal of Heat and Fluid Flow 97, 109029 (2022).
- ²³M. P. Buckley and F. Veron, "Airflow measurements at a wavy air-water interface using piv and lif," Experiments in Fluids 58, 1–20 (2017).
- ²⁴J. M. Wallace, H. Eckelmann, and R. S. Brodkey, "The wall region in turbulent shear flow," Journal of Fluid Mechanics **54**, 39–48 (1972).
- ²⁵Y. Odemark and J. H. Fransson, "The stability and development of tip and root vortices behind a model wind turbine," Experiments in fluids **54**, 1–16 (2013)
- ²⁶M. Calaf, C. Meneveau, and J. Meyers, "Large eddy simulation study of fully developed wind-turbine array boundary layers," Physics of fluids 22 (2010).
- ²⁷R. Barthelmie, O. F. Hansen, K. Enevoldsen, J. Højstrup, S. Frandsen, S. Pryor, S. Larsen, M. Motta, and P. Sanderhoff, "Ten years of meteorological measurements for offshore wind farms," J. Sol. Energy Eng. 127, 170–176 (2005).
- ²⁸M. Türk and S. Emeis, "The dependence of offshore turbulence intensity on wind speed," Journal of Wind Engineering and Industrial Aerodynamics 98, 466–471 (2010).
- ²⁹J. Counihan, "Adiabatic atmospheric boundary layers: a review and analysis of data from the period 1880–1972," Atmospheric Environment (1967) 9, 871–905 (1975).
- ³⁰O. Ferčák, "Experimental particle image velocimetry (piv) data for mouchref 2024," https://github.com/ofercak/turbulence-quantification-of-reynolds-shear-stress-wave-phase-dependence (2024).
- ³¹Z. Yang, P. Sarkar, and H. Hu, "Visualization of the tip vortices in a wind turbine wake," Journal of visualization 15, 39–44 (2012).
- ³²S. J. Andersen, J. N. Sørensen, and R. F. Mikkelsen, "Turbulence and entrainment length scales in large wind farms," Philosophical Transactions of the Royal Society A: Mathematical, Physical and Engineering Sciences 375, 20160107 (2017).
- ³³M. Raupach, "Conditional statistics of reynolds stress in rough-wall and smooth-wall turbulent boundary layers," Journal of Fluid Mechanics 108, 363–382 (1981).
- ³⁴D. Poggi, G. Katul, and J. Albertson, "Momentum transfer and turbulent kinetic energy budgets within a dense model canopy," Boundary-Layer Meteorology 111, 589–614 (2004).
- ³⁵K. Thomsen and P. Sørensen, "Fatigue loads for wind turbines operating in wakes," Journal of Wind Engineering and Industrial Aerodynamics 80, 121–136 (1999).